Shear deformation-induced anisotropic thermal conductivity of graphene

Liu Cui [1, 2], Sanqiang Shi [2, †], Gaosheng Wei [1], Xiaoze Du [1, †]

[1]*Key Laboratory of Condition Monitoring and Control for Power Plant Equipments of Ministry of Education, North China Electric Power University, Changping, Beijing 102206, China*

[2]*Department of Mechanical Engineering, The Hong Kong Polytechnic University, Hung Hom, Kowloon, Hong Kong, China*

[†] To whom correspondence should be addressed.

E-mail: mmsqshi@polyu.edu.hk (S. Shi); duxz@ncepu.edu.cn (X. Du)

Abstract

Graphene-based materials exhibit intriguing phononic and thermal properties. In this paper, we have investigated the heat conductance in graphene sheets under shear-strain-induced wrinkling deformation, using equilibrium molecular dynamics simulations. A significant orientation dependence of thermal conductivity of graphene wrinkle (GW) is observed. The directional dependence of thermal conductivity of GW stems from the anisotropy of phonon group velocities as revealed by the G-band broadening of phonon density of states (DOS), the anisotropy of thermal resistances as evidenced by the G-band peak mismatch of phonon DOS, and the anisotropy of phonon relaxation time as a direct result of the double-exponential-fitting of heat current autocorrelation function. By analyzing the relative contributions of different lattice vibrations to heat flux, we have shown that the contributions of different lattice vibrations to heat flux of GW are sensitive to the heat flux direction, which further indicates the orientation-dependent thermal conductivity of GW. Moreover, we have found that, in the strain range of 0-0.1, the anisotropy ratio of GW increases monotonously with increasing shear strain. It is induced by the change in the number of wrinkles, which is more influential in the direction perpendicular to the wrinkle texture. The findings elucidated here emphasize the utility of wrinkle engineering for manipulation of nanoscale heat transport, which offers opportunities for the development of thermal channeling devices.

1. Introduction

Heat conduction in low dimensional structures has become a hot topic in condensed matter physics, inspired by the developments of electronics and phononics. Among various nanomaterials, graphene, a planar single sheet of sp^2-bonded carbon atoms arranged in a honeycomb lattice [1], gains particular interest. Its ultra-high thermal conductivity [2, 3] has motivated many efforts to tailoring graphene thermal properties to meet the particular needs of different applications, such as thermoelectrics [4-8], thermal management [3, 9], thermal rectification [10, 11] and thermal cloaking [12].

As numerous studies have confirmed, the thermal properties of graphene can be modified by various strategies, including chemical functionalizations [13, 14], structural defects [15, 16], substrate interactions [17, 18], strain-induced deformations [19-21], etc. It should be pointed out that the strain-induced deformation could be one of the most promising methods because it does not break the pristine structure, and hence induces reversible changes in graphene properties. Shear strain has been found to cause the formation of wrinkles in graphene. These wrinkles go across the entire graphene sheet with a well-defined direction [22, 23]. Recent developments in fabrication techniques, such as cooperating with substrate morphology [24], thermally and atomic force microscopy tips induced compression [25-27], make it possible to manipulate the conformation of graphene wrinkles (GWs) intentionally.

While the experimental measurement of thermal conductivity on the nanoscale is technically difficult, the molecular dynamics (MD) simulation is extensively used to investigate the heat transport in GWs. Shen [20] simulated GW thermal conductivity by

using equilibrium MD (EMD). He found that GWs exhibit a significant reduction in thermal conductivity as compared with the pristine graphene. Similarly reduced thermal conductivity of GW was also demonstrated in our previous investigations based on non-equilibrium MD (NEMD) simulations [21]. However, Zhang et al. [28] in their NEMD study reported that the heat conduction in graphene is not sensitive to shear deformation. The thermal conductivity of graphene nanoribbon with strain-induced wrinkles decreases only 12% and 16% in zigzag and armchair directions, respectively. Different from the complete GW structure investigated in the above noted references, a specific wrinkling strip was selected by Wang et al. [19] to analyze the wrinkle effect. Their NEMD results indicate that wrinkles have little effect on the thermal conductivity along the wrinkling direction, while playing an important role in the reduction of thermal conductivity along the texture direction. Up to now, only limited investigations have been performed to understand the wrinkle effect on graphene thermal conduction, and their conclusions are inconsistent. Both the strain and wrinkling configuration may induce changes in physical properties. The physical origin of the tunable and direction-dependent heat transport in GWs is still an open question.

In this paper, we study the heat transport in GWs by using EMD simulations. The results confirm a high anisotropy of GW heat conduction. Furthermore, we calculate the phonon density of states in different directions and different regions, the phonon relaxation time and the contributions of lattice vibrations in different directions to heat flux to explore the underlying mechanisms behind the anisotropic thermal conductance of GW.

2. Model and methodology

The GWs were constructed by applying shear strain to graphene sheets. Fig. 1(a) depicts one rectangular graphene sheet with length L=30 nm and width W=30 nm. The atoms in the bottommost row were fixed, and the shear displacement along the horizontal direction was exerted on atoms in the topmost row. Herein, the timestep was taken as 0.5 fs, and the loading rate was set to 0.03 nm (shear strain 0.001) per 20000 time steps. The larger the accumulated displacement, the higher the shear strain applied to graphene. It is observed that the GW configuration can be kept stable until the shear strain is up to 0.174. To get global minimum energy configurations of graphene and GW, a simulated annealing process was further performed. The annealing simulation is allowed to explore conformation space for low energy structures by periodically increasing and then decreasing the temperature of a classical dynamic trajectory to avoid trapping the structure in a conformation that represents a local energy minimum. During the annealing, the system was heated from 300 K to 800 K at an interval of 50 K and then cooled back at an interval of 50 K. At each step of annealing, 100 ps NPT ensemble with a time step of 0.5 fs was applied on the system. The temperature and pressure were retained by the Nose-Hoover thermostat and barostat [29, 30], respectively. The obtained atomic configurations of graphene and GW under shear strain 0.1 are shown in Fig. 1(b) and (c), respectively. For the graphene sheet presented in Fig. 1(b), its structure is not perfectly flat but displays intrinsic microscopic roughening, which is in good agreement with the experimental observation [31]. The GW structure shown in

Fig. 1(c) is characterized by two important parameters: the mean wrinkle amplitude of 0.877 nm and wavelength of 4.111 nm.

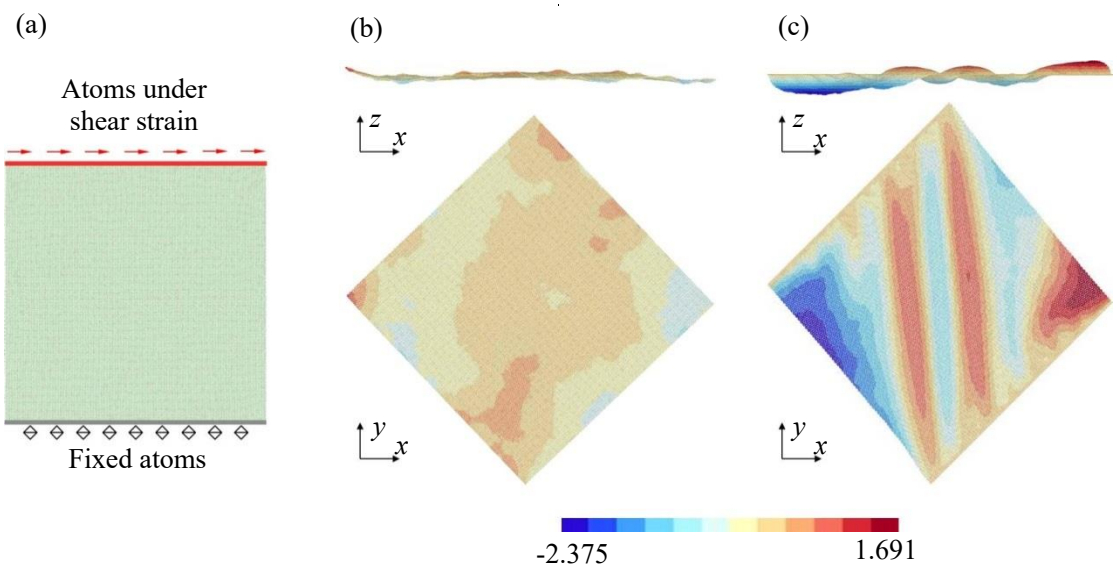

Figure 1. Initial configuration of graphene (a), minimal energy configurations of graphene (b) and graphene wrinkle under shear strain 0.1 (c). Different colors in figures (b) and (c) indicate different *z*-coordinate values of carbon atoms.

The EMD method was performed to calculate the thermal conductivity. It has been successfully applied for the prediction of thermal properties of nanostructured materials [32-35]. In the EMD simulations, the thermal conductivity is estimated using the Green-Kubo formula [36], which relates the ensemble average of autocorrelation of heat flux to the thermal conductivity

$$\lambda = \frac{1}{k_{\mathrm{B}} T^2 V} \int_0^{\infty} < J(0) J(t) > \mathrm{d}t \qquad (1)$$

where k_{B} is Boltzmann's constant. V and T are the system volume and temperature, respectively. Angular brackets denote the ensemble average. $J(t)$ is the heat flux at time t and defined by

$$J(t) = \sum_i E_i v_i - \sum_i S_i v_i \quad (2)$$

where v, E, S are the velocity, total energy and symmetric stress tensor of atom i, respectively.

In this work, the AIREBO potential [37] was used to describe the interatomic interactions. All MD calculations were carried out using LAMMPS [38] with a timestep of 0.5 fs throughout. Free boundary conditions were applied in all directions. The system was initially equilibrated in the NVT ensemble using the Nosé-Hoover thermostat for 2 ns. Then, the system evolves in the NVE ensemble for another 2 ns, in which the first 1 ns was used to relax the system, while the next 1 ns to record the heat flux. Each value of GW thermal conductivity was evaluated from 6 independent 50-ps Green-Kubo integrations.

3. Results and discussion

3.1 Anisotropic thermal conductivity

The calculated thermal conductivities of graphene and GW under shear strain 0.1 are compared in Fig. 2. It can be seen that the thermal conductivities of graphene at 300 K are 180.64 and 178.90 $Wm^{-1}K^{-1}$ along the x- and y-axis, respectively. This in-plane isotropy of heat transport agrees well with the common understanding of graphene thermal properties. Fig. 2 also shows that the wrinkles could significantly degrade the heat conduction property of graphene. As noted in our previous study [21], the suppression in GW thermal conductivity could be attributed to the strong phonon localizations and enhanced phonon scatterings. Furthermore, as shown in Fig. 2, the in-plane heat

transport of GW exhibits anisotropic behavior. The thermal conductivity value along *y*-axis is about 1.56 times larger than that along *x*-axis. Similar behavior has also been found in phosphorene [39], whose thermal conductance in the zigzag direction is about 40% larger than that in the armchair direction due to its unique puckered structure. The highly anisotropic thermal conductance of GW is beneficial for the design and control of thermal channeling devices, thus showing another important utilization of GWs besides their applications in thermoelectrics.

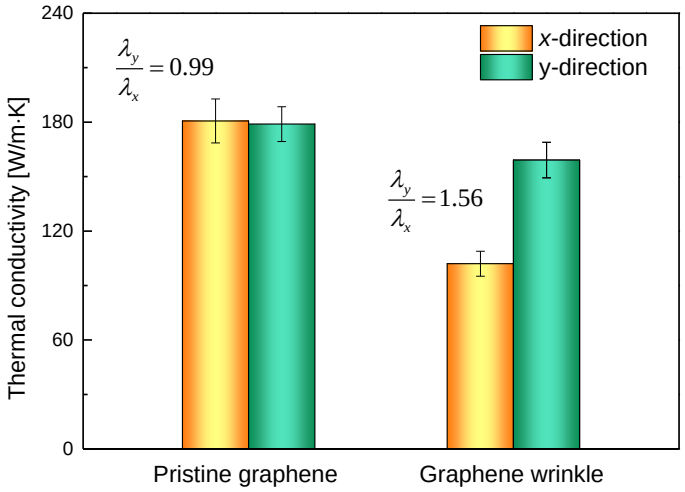

Figure 2. Thermal conductivity of pristine graphene and graphene wrinkle under 300 K.

3.2 Phonon density of states

To elucidate the underlying mechanisms for the anisotropic thermal conductivity, the phonon density of states (DOS) was calculated by taking the Fourier transform of velocity autocorrelation function (VACF) [40, 41]. For an ensemble of *N* atoms, the VACF is defined as

$$\mathrm{VACF}(t)=\left\langle \frac{1}{N}\sum_{i=1}^{N}\vec{v}_i(t_0)\cdot\vec{v}_i(t_0+t)\right\rangle \tag{3}$$

where $\vec{v}_i(t_0)$ denotes the velocity of i-th atom at time t_0. The expression of DOS is

$$\mathrm{DOS}(v) = \int_{-\infty}^{+\infty} \mathrm{VACF}(t)\mathrm{e}^{-2\pi ivt}\mathrm{d}t \tag{4}$$

in which v is the phonon frequency.

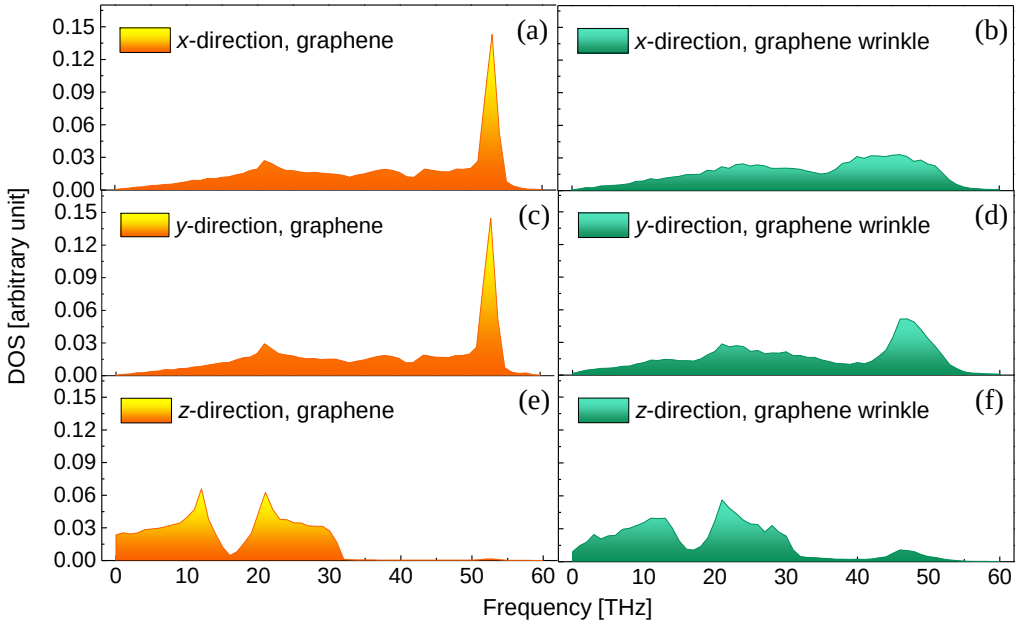

Figure 3. Phonon density of states for pristine graphene and graphene wrinkle.

Fig. 3 shows the polarized DOS of graphene and GW under shear strain 0.1 The reported DOS of graphene is consistent with the previous study [42], which illustrates that the high frequency range is dominated by the in-plane phonon modes whereas the out-of-plane modes concentrate on the low frequency range. Wang et al. [19] deduced that the configuration of wrinkles changes the 2D atomic monolayer structure to the 3D configuration and gives much stronger phonon scattering along the out-of-plane direction. However, the polarized DOS gives rise to different answers. As shown in Fig. 3 (e) and (f), there is no obvious difference between the out-of-plane DOS of graphene and GW. It reveals that the out-of-plane phonon spectrum is slightly affected by the wrinkling configuration, although the graphene undergoes out-of-plane buckling under

shear strain. For the DOS of in-plane modes shown in Fig. 3 (a)-(d), the noticeable effect of shear strain is a broadening of G-band originating from some high-frequency bands that are red-shifted with respect to the graphene G-band. It induces the reduction in phonon group velocities, and thus the decrease in thermal conductivity of GW. Moreover, an anisotropy is observed in the in-plane DOS of GW. The softening of G-band in the *x*-direction is much stronger than that in the *y*-direction. It indicates that the shear strain have different impacts on phonon group velocities of two types of in-plane phonons. This may be related to the directional dependence of thermal conductance in GW.

In order to gain more physical insight into the anisotropic thermal conductivity, we compared the DOS in different regions of GW. The shear strain causes the wrinkles in graphene, which modify the local bond lengths of carbon atoms. Herein, we divided the GW into two regions (i.e. the crest/trough region and the joint region) as shown in the inset of Fig. 4. The average bond lengths between carbon atoms in the crest/trough and joint regions are 1.435 Å and 1.416 Å, respectively. The calculated DOS of the crest/trough and joint are illustrated in Fig. 4. In the *y*-direction, we found that the DOS of carbon atoms in the crest/trough region is similar to that in the joint region with a G-band peak at about 47 THz. Differently, in the *x*-direction, the G-band peak of DOS of the joint displays a redshift in comparison with that of the crest/trough. Unlike the DOS in the *y*-direction, there is a large mismatch in DOS peaks in the *x*-direction, which indicates a large interfacial thermal resistance between the atoms in crest/trough and joint regions. As shown in the inset of Fig. 4, the atoms in the crest/trough and joint

regions are parallel to one another along the *y*-axis; nevertheless, they are arranged alternatively along the *x*-axis. The heat transfer in the *y*-direction is thus accomplished through these parallel heat channels, thereby being relatively more efficient. However, the heat is transported along the *x*-axis by the atoms in crest/trough and joint regions alternatively, in a similar manner to that in superlattice structures [43, 44]. The large thermal resistance is responsible for the lower thermal conductivity in the *x*-direction.

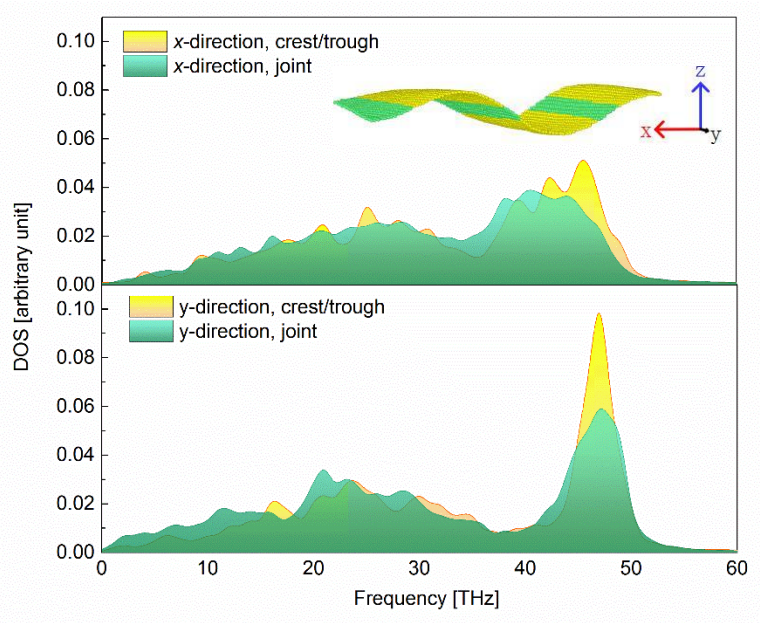

Figure 4. Phonon density of states for carbon atoms in the crest/trough and joint regions of graphene wrinkle. The inset illustrates the partial structure of graphene wrinkle. The yellow and green atoms represent the crest/trough and joint regions, respectively.

3.3 Phonon relaxation time

The mechanism of anisotropic thermal conductivity of GW is further discussed via the phonon relaxation time, which can be extracted from the heat current autocorrelation function (HCACF). Fig. 5 shows the calculated HCACF of graphene and GW under

shear strain 0.1. It can be seen that the HCACFs are characterized by a rapid initial decay followed by a gradual exponential decay over a long time. The rapid decay reflects the contribution of optical phonons to thermal conductivity, while the slower decay corresponds to the contribution from acoustic phonons. As suggested by Che et al. [45], the decay curve of HCACF can be fitted by a double exponential function

$$\mathrm{HCACF}(t) = A_{\mathrm{o}} \exp\left(-t/\tau_{\mathrm{o}}\right) + A_{\mathrm{a}} \exp\left(-t/\tau_{\mathrm{a}}\right) \tag{5}$$

where the subscripts o and a denote optical and acoustic modes, respectively. A_{o}, τ_{o}, A_{a} and τ_{a} are the fitting parameters derived using a nonlinear least-square method. τ_{o} and τ_{a} correspond to the relaxation time of optical and acoustic phonons, respectively. According to Eq. (1), the thermal conductivity can be obtained as

$$\lambda = \frac{1}{k_{\mathrm{B}} T^2 V}\left(A_{\mathrm{o}}\tau_{\mathrm{o}} + A_{\mathrm{a}}\tau_{\mathrm{a}}\right) \tag{6}$$

The fitting results of graphene and GW are listed in Table 1. It is clearly seen that both τ_{o} and τ_{a} of pristine graphene are weakly direction-dependent. Moreover, the acoustic phonons exert a greater influence on the graphene thermal conductance, with the acoustic phonons accounting for 98.75% of the thermal conductivity. Different characteristics are observed in the GW as illustrated in Table 1. In contrast to the similar values of τ_{o} along the *x*- and *y*-directions, τ_{a} of GW along the *y*-direction is much larger than that along the *x*-direction. Table 1 also suggests that the contribution of acoustic phonons slightly decreases due to the introduction of wrinkles, with 3.91% and 5.25% reduction along the *x*- and *y*-directions, respectively. The acoustic phonons are still the dominant heat carriers in GWs. The above comparison reveals that the large difference in relaxation time for acoustic phonons along the *x*- and *y*-directions may explain the

strong anisotropy in thermal conductivity of GWs.

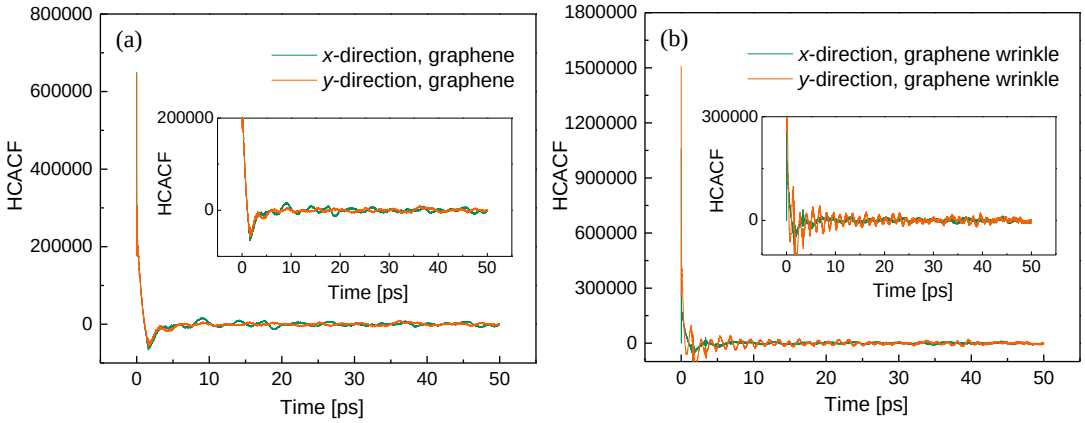

Figure 5. Heat current autocorrelation functions for pristine graphene (a) and graphene wrinkle (b).

Table 1. Curve-fit parameters of heat current autocorrelation functions for pristine graphene and graphene wrinkle.

	A_o	τ_o (ps)	A_a	τ_a (ps)	λ_o (%)	λ_a (%)
Graphene						
x-direction	400000	0.00366	294695	0.39353	1.25	98.75
y-direction	400000	0.00362	302068	0.37786	1.25	98.75
Graphene wrinkle						
x-direction	1000000	0.00368	259975	0.26000	5.16	94.84
y-direction	2000000	0.00376	319314	0.33871	6.50	93.50

3.4 Contributions of lattice vibrations

To obtain more information about the underlying mechanism for the anisotropic thermal conductivity of GW, the relative contributions of different lattice vibrations to total heat flux were estimated by [46]

$$J_{\mathrm{A}\to\mathrm{B},\alpha} = -\frac{1}{2S}\sum_{i\in\mathrm{A}}\sum_{j\in\mathrm{B}} F_{ij\alpha}\left(\upsilon_{i\alpha}+\upsilon_{j\alpha}\right) \tag{7}$$

where $J_{\mathrm{A}\to\mathrm{B},\alpha}$ is the heat flux across a virtual interface (located at the middle of the structure, by which the atoms splits into two groups, i.e. “A” and “B” groups) due to

the lattice vibrations in the α direction. S is the cross-sectional area. $F_{ij\alpha}$ is the α component of the force acting on atom i due to atom j. $v_{i\alpha}$ is the α component of the velocity of atom i. Noted that the system based on EMD simulation has an average heat flux of zero which cannot be used for further analysis. Hence, $J_{A\rightarrow B,\alpha}$ was estimated from the NEMD simulation with tersoff potential [47, 48], in which the average heat flux is a nonzero constant. The NEMD calculation used the same structure model as EMD. Two thermostatted regions were built at opposite ends of the graphene or GW. By holding these two regions at different temperatures, a steady heat flux was obtained. Moreover, it is necessary to point out that the formula (7) is based on two-body interactions. Although the Tersoff potential involves three-body terms, it has been demonstrated that they can be decomposed into two-body components [46].

Figure 6 shows the directional contribution to the total heat flux of graphene and GW. For graphene, as seen from Fig. 6 (a), the lattice vibration in x-direction has the largest contribution to the heat flux along the direction perpendicular to the wrinkle texture (J_x), while the lattice vibration in y-direction contributes most to the heat flux along the direction parallel to the wrinkle texture (J_y). It indicates that the lattice vibration along the heat conduction direction provides the main contribution. Similar conclusions have been reported by Ye et al. for graphene nanoribbons [49] and Zeraati et al. for arsenene [50]. Fig. 6 (b) shows that the wrinkles affect the in-plane phonon transport significantly. For both J_x and J_y of GW, in comparison with those of graphene, the contribution from the lattice vibration in x-direction is reduced while that from the lattice vibration in y-direction is enhanced. Most of J_y of GW is still contributed by the lattice vibration in

y-direction. However, for J_x of GW, the dominant contribution changes from the lattice vibration in *x*-direction to that in *y*-direction. Such changes in directional contributions to J_x and J_y may account for the anisotropic thermal conductivity of GW.

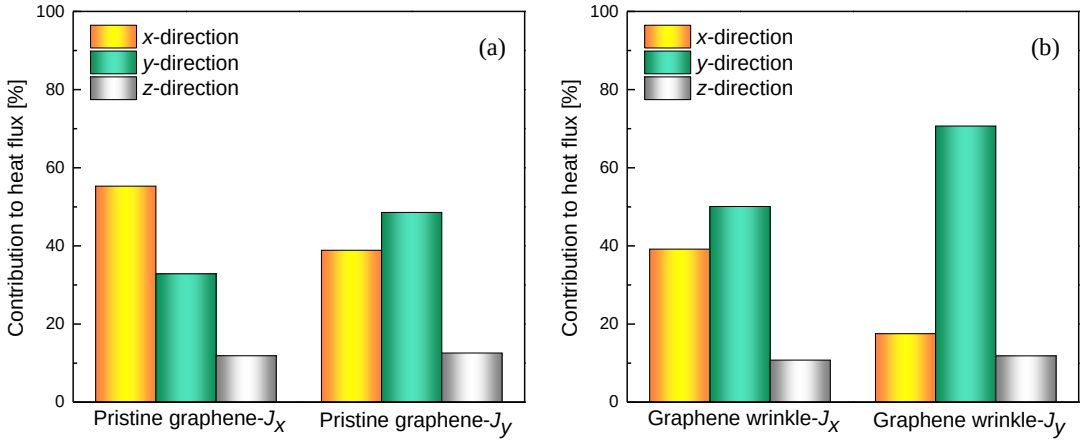

Figure 6. Contributions of lattice vibrations to the total heat flux of graphene (a) and graphene wrinkle (b).

It should be noted that the contributions of different phonon vibration modes to heat transport in graphene still remain unclear. Numerous theoretical studies [17, 51-58] have investigated the relative importance of each phonon vibration mode by using both Boltzmann transport equation (BTE) and MD approaches. Currently, there are two conflicting views of the role of out-of-plane phonons: the dominant carriers [17, 54, 55] versus the non-dominant carriers [51, 53, 56-58]. Our results demonstrate that the in-plane phonons, rather than the out-of-plane phonons, contribute most to heat conduction of graphene. It may be attributed to the finite length effect. For the graphene sample with length of 30 nm and width of 30 nm, the long-wavelength out-of-plane phonons are scattered on sample boundaries and their dominant role in the heat transfer processes may be eliminated. We hope that this work can motivate additional theoretical and experimental studies to shed light on relative contributions from different phonons to

thermal conductivity of graphene materials.

3.5 Effect of shear strain

The shear strain effect on thermal conductivity is further studied to provide guidelines for the utilization of GW. The thermal conductivity and the anisotropy ratio (λ_y/λ_x) of GW under different shear strain ranging from 0 to 0.1 are shown in Fig. 7 (a). It is clearly seen that the thermal conductivity along both *x*- and *y*-directions decreases as the shear strain increasing. Interestingly, the thermal conductivity of GW in the *x*-direction is more sensitive to the shear strain than that in the *y*-direction. In the strain range of 0-0.1, the anisotropy ratio of GW increases monotonously with increasing shear strain. This may be attributed to the change in strain-induced deformations. As mentioned previously, there is a large interfacial thermal resistance between the atoms in crest/trough and joint regions, as demonstrated by DOS shown in Fig. 4. As shown in Fig. 7 (b), an increment in the shear strain increases the number of wrinkles, which leads to an increment in the number of interfaces between the crest/trough region and joint region. When phonons transport along *x*-axis, they cross more interfaces. As a result, the probability of phonon-interface scattering increases, and the thermal conductivity in the *x*-direction will reduce significantly. However, when phonons transport along *y*-axis, their movements are parallel to the interfaces. The interfaces have little influence on the phonon transport along *y*-direction, which means that the thermal conductivity along the *y*-direction is relatively lightly affected by the interface number. This helps to explain why the shear strain has less influence on the thermal

conduction along the *y*-direction in comparison with that along the *x*-direction.

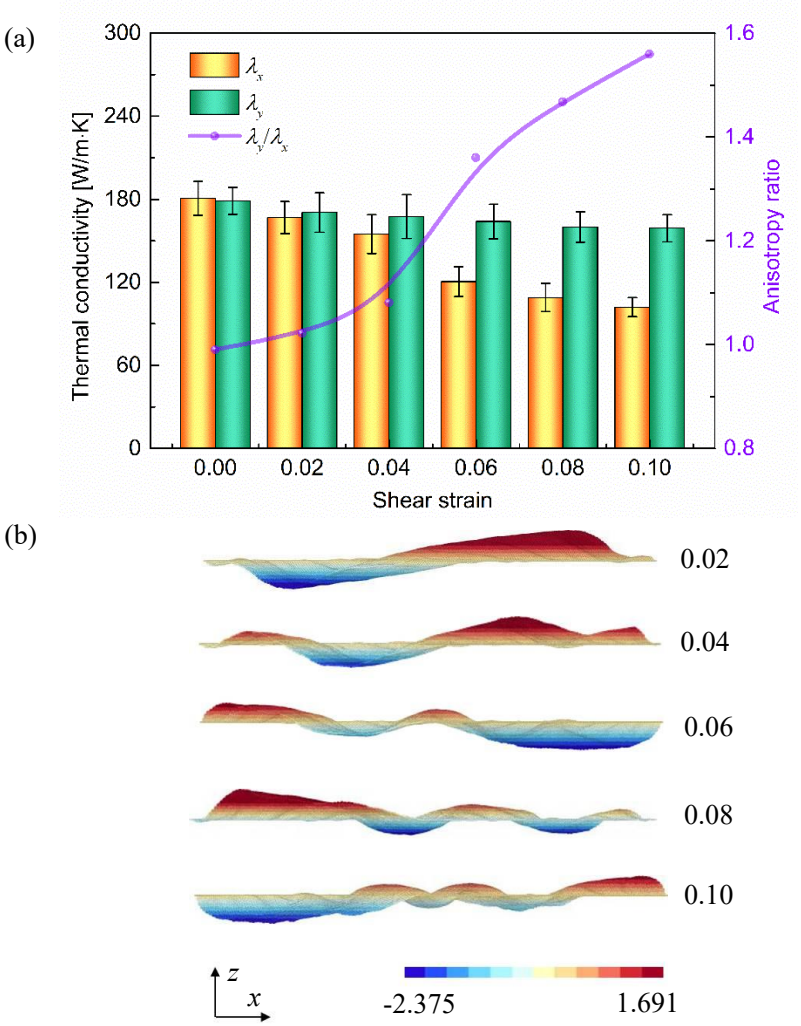

Figure 7. Thermal conductivity and anisotropy ratio of graphene wrinkle under different shear strain (a). Atomic configurations of graphene wrinkles under different shear strain (b). Different colors in figure (b) indicate different *z*-coordinate values of carbon atoms.

4. Conclusions

The thermal conductivity of graphene under shear-strain-induced wrinkling deformation has been investigated by using EMD simulations with AIREBO potential. In contrast to the isotropic in-plane thermal conductivity of graphene, the thermal transport in GWs exhibits a strong anisotropy, with an anisotropy ratio of 1.56 for the

GW under shear strain 0.1. The main origin of orientation-dependent thermal conductivity lies in the anisotropy of phonon group velocity, phonon relaxation time and thermal resistance. The contributions of different lattice vibrations to heat flux of GW are sensitive to the heat flux direction, which further indicates the orientation dependence of thermal conductivity of GW. In the strain range of 0-0.1, the anisotropy ratio of GW increases monotonously with increasing shear strain. It is attributed to the change in the number of wrinkles. The present work highlights the potential of GW applications for thermal channeling devices.

Acknowledgements

The authors are thankful for financial support from the Hong Kong Scholars Program (No. XJ2016042), China Postdoctoral Science Foundation Funded Project (No. 2016M600980), National Natural Science Foundation of China (No. 51741604, 51676069 and 51376060) and Fundamental Research Funds for the Central Universities (No. 2015ZZD09).

References

1. A. K. Geim and K. S. Novoselov, *Nature Materials*, 2007, 6, 183-191.
2. A. A. Balandin, S. Ghosh, W. Bao, I. Calizo, D. Teweldebrhan, F. Miao and C. N. Lau, *Nano Letters*, 2008, 8, 902-907.
3. S. Ghosh, I. Calizo, D. Teweldebrhan, E. P. Pokatilov, D. L. Nika, A. A. Balandin, W. Bao, F. Miao and C. N. Lau, *Applied Physics Letters*, 2008, 92, 151911.
4. Y. M. Zuev, W. Chang and P. Kim, *Physical Review Letters*, 2009, 102, 096807.
5. X. Ni, G. Liang, J. Wang and B. Li, *Applied Physics Letters*, 2009, 95, 192114.

6. H. Sevinçli and G. Cuniberti, *Physical Review B*, 2010, 81, 113401.
7. G. A. Nemnes, C. Visan and A. Manolescu, *Journal of Materials Chemistry C*, 2017, 5, 4435-4441.
8. A. Reshak, S. A. Khan and S. Auluck, *Journal of Materials Chemistry C*, 2014, 2, 2346-2352.
9. M. H. Bae, Z. Y. Ong, D. Estrada and E. Pop, *Nano Letters*, 2010, 10, 4787-4793.
10. J. Hu, X. Ruan and Y. P. Chen, *Nano Letters*, 2009, 9, 2730-2735.
11. N. Yang, G. Zhang and B. Li, *Applied Physics Letters*, 2009, 95, 033107.
12. P. Y. Chen and A. Alù, *ACS Nano*, 2011, 5, 5855-5863.
13. S. K. Chien, Y. T. Yang and C. K. Chen, *Applied Physics Letters*, 2011, 98, 033107.
14. Q. Pei, Z. Sha and Y. Zhang, *Carbon*, 2011, 49, 4752-4759.
15. Z. G. Fthenakis, Z. Zhu and D. Tománek, *Physical Review B*, 2014, 89, 125421.
16. G. Rajasekaran, P. Narayanan and A. Parashar, *Critical Reviews in Solid State and Materials Sciences*, 2016, 41, 47-71.
17. J. H. Seol, I. Jo, A. L. Moore, L. Lindsay, Z. H. Aitken, M. T. Pettes, X. Li, Z. Yao, R. Huang and D. Broido, *Science*, 2010, 328, 213-216.
18. A. France-Lanord, P. Soukiassian, C. Glattli and E. Wimmer, *Physical Review Applied*, 2017, 7, 034030.
19. C. Wang, Y. Liu, L. Li and H. Tan, *Nanoscale*, 2014, 6, 5703-5707.
20. H. Shen, *Molecular Simulation*, 2015, 41, 231-236.
21. L. Cui, X. Du, G. Wei and Y. Feng, *The Journal of Physical Chemistry C*, 2016, 120, 23807-23812.
22. A. Fasolino, J. Los and M. I. Katsnelson, *Nature Materials*, 2007, 6, 858-861
23. C. Wang, Y. Liu, L. Lan and H. Tan, *Nanoscale*, 2013, 5, 4454-4461.
24. Z. Pan, N. Liu, L. Fu and Z. Liu, *Journal of the American Chemical Society*, 2011, 133, 17578-17581.
25. Z. Li, Z. Cheng, R. Wang, Q. Li and Y. Fang, *Nano Letters*, 2009, 9, 3599-3602.
26. W. Bao, F. Miao, Z. Chen, H. Zhang, W. Jang, C. Dames and C. N. Lau, *Nature Nanotechnology*, 2009, 4, 562-566.
27. A. P. M. Barboza, H. Chacham, C. K. Oliveira, T. F. D. Fernandes, E. H. M. Ferreira, B. S. Archanjo, R. J. C. Batista, A. B. de Oliveira and B. R. A. Neves, *Nano Letters*, 2012, 12, 2313-2317.
28. C. Zhang, X. Hao, C. Wang, N. Wei and T. Rabczuk, *Scientific Reports*, 2017, 7, 41398
29. S. Nosé, *The Journal of Chemical Physics*, 1984, 81, 511-519.
30. W. G. Hoover, *Physical Review A*, 1985, 31, 1695.
31. J. C. Meyer, A. K. Geim, M. I. Katsnelson, K. S. Novoselov, T. J. Booth and S. Roth, *Nature*, 2007, 446, 60-63.
32. Y. Hong, J. Zhang and X. C. Zeng, *The Journal of Physical Chemistry C*, 2016, 120, 26067-26075.
33. X. Qian, X. Gu and R. Yang, *The Journal of Physical Chemistry C*, 2015, 119, 28300-28308.

34. L. Cui, Y. Feng and X. Zhang, *Physical Chemistry Chemical Physics*, 2015, 17, 27520-27526.
35. T. Zhang and L. Zhu, *Physical Chemistry Chemical Physics*, 2017, 19, 1757-1761.
36. P. K. Schelling, S. R. Phillpot and P. Keblinski, *Physical Review B*, 2002, 65, 144306.
37. S. J. Stuart, A. B. Tutein and J. A. Harrison, *The Journal of Chemical Physics*, 2000, 112, 6472-6486.
38. S. Plimpton, *Journal of Computational Physics*, 1995, 117, 1-19.
39. Z. Ong, Y. Cai, G. Zhang and Y. Zhang, *The Journal of Physical Chemistry C*, 2014, 118, 25272-25277.
40. G. S. Grest, S. R. Nagel, A. Rahman and T. A. Witten Jr, *The Journal of Chemical Physics*, 1981, 74, 3532-3534.
41. X. Wang, Y. Hong, D. Ma and J. Zhang, *Journal of Materials Chemistry C*, 2017, 5, 5119-5127.
42. Y. Hong, J. Zhang, X. Huang and X. C. Zeng, *Nanoscale*, 2015, 7, 18716-18724.
43. X. Mu, T. Zhang, D. B. Go and T. Luo, *Carbon*, 2015, 83, 208-216.
44. X. Wang, Y. Hong, P. K. Chan and J. Zhang, *Nanotechnology*, 2017, 28, 255403.
45. J. Che, T. Çağın, W. Deng and W. A. Goddard III, *The Journal of Chemical Physics*, 2000, 113, 6888-6900.
46. X. Zhang, M. Hu and D. Tang, *Journal of Applied Physics*, 2013, 113, 147.
47. J. Tersoff, *Physical Review B*, 1989, 39, 5566.
48. J. Tersoff, *Physical Review B*, 1990, 41, 3248.
49. Z. Ye, B. Cao, W. Yao, T. Feng and X. Ruan, *Carbon*, 2015, 93, 915-923.
50. M. Zeraati, S. M. V. Allaei, I. A. Sarsari, M. Pourfath and D. Donadio, *Physical Review B*, 2016, 93, 085424.
51. L. Chen and S. Kumar, *Journal of Applied Physics*, 2012, 112, 043502.
52. Z. Y. Ong and E. Pop, *Physical Review B*, 2011, 84, 075471.
53. Z. Wei, J. Yang, K. Bi and Y. Chen, *Journal of Applied Physics*, 2014, 116, 153503.
54. L. Lindsay, D. A. Broido and N. Mingo, *Physical Review B*, 2010, 82, 115427.
55. D. Singh, J. Y. Murthy and T. S. Fisher, *Journal of Applied Physics*, 2011, 110, 044317.
56. P. G. Klemens, *Journal of Wide Bandgap Materials*, 2000, 7, 332-339.
57. P. G. Klemens, *International Journal of Thermophysics*, 2001, 22, 265-275.
58. P. G. Klemens and D. F. Pedraza, *Carbon*, 1994, 32, 735-741.